3D Printed Loop Heat Pipes for High-Performance Small Satellites

Rohit Gupta, Chien-Hua Chen, William G. Anderson
Advanced Cooling Technologies, Inc.
1046 New Holland Ave, Lancaster, PA 17601; 717-295-6061
rohit.gupta@1-act.com

ABSTRACT

Advanced Cooling Technologies has been developing 3D printed loop heat pipes as low-cost, rapidly-manufacturable alternatives to standard loop heat pipes. With 3D printing, the evaporator build can be entirely automated leading to significant savings in costs and lead times. The 3D printed loop heat pipe can enable high-performance small satellites with significant enhancement of the heat rejection capability. This paper provides a comprehensive narrative of the 3D printed loop heat pipe development, including an exposition of the wick and evaporator development, and a discussion of select test results acquired in the laboratory. The evaporator wick was achieved by carefully controlling the build parameters in laser powder bed fusion to force incomplete melting of the stainless-steel powder. The evaporator was developed as a single bi-porous part, containing a wick section that is surrounded by an annular wall, requiring zero post-build assembly. The 3D printed loop heat pipes were successfully operated in the laboratory with both propylene and ammonia, including at a heat load of over 300 W with the latter working fluid. A purpose-built propylene 3D printed loop heat pipe for NASA's VIPER EDU was also demonstrated successfully, leading to a TRL 6 advancement for the technology.

INTRODUCTION

Advanced Cooling Technologies, Inc. (ACT) has been developing 3D Printed Loop Heat Pipes (3DP-LHPs) with NASA SBIR funding. The 3DP-LHP is a low-cost, rapidly-manufacturable alternative to standard Loop Heat Pipe (LHP), which exploits additive manufacturing to eliminate high-risk, labor-intensive manufacturing processes. These labor-intensive steps include the wick fabrication, vapor groove machining, wick insertion, knife-edge sealing, etc. With 3D printing, the evaporator can be built as a single part with all the necessary subcomponents. This enables complete automation of the evaporator fabrication, including the elimination of any assembly needs, leading to over 50% savings in cost and lead time.

The 3DP-LHP can enable high-performance small satellites (SmallSats) for communications, remote sensing, etc. with significant commercial impact. The performance of SmallSats is currently hindered by the low heat rejection capability of low-cost LHP alternatives, such as thermal straps. The 3DP-LHP can significantly enhance the heat rejection capability of SmallSats through the addition of deployable radiators. Thus, large satellite missions can potentially be achieved within SmallSat SWaP-C through the use of the 3DP-LHP. Moreover, 3D printing offers significant design freedom that can lead to a simplification of the SmallSat design process. Beyond earth-based application, the 3DP-LHP can also enable low-cost and high-performance lunar and Martian spacecraft of the future.

The various stages of development of the ACT 3DP-LHP have been documented in previous publications.[1–3] This paper provides a comprehensive narrative of ACT's 3DP-LHP development, including an exposition of the wick and evaporator development and a discussion of results from select baseline testing conducted in the laboratory. The paper also discusses a propylene 3DP-LHP that was purpose-built for NASA's VIPER EDU testing.

METHODS

Laser Powder Bed Fusion

The wick samples and evaporators were built using Laser Powder Bed Fusion of standard spherical 316L SS powder. The porous, wick sections were built by preventing a complete fusion of the powder through control of the build parameters, i.e., the power, exposure time, point distance, hatch spacing, and layer thickness. These parameters are combined into a custom, compact variable called the energy density, E_ρ, which has units of J/mm^3. Similar strategies for porous wick development have also been attempted in the literature.[4,5]

A CAD rendering and photograph of the samples used for the wick development are presented in Figure 1. The sample features a bi-porous, single part construction with a porous cylindrical section that is surrounded by a

solid, annular wall. This design was selected with the goal of realizing evaporators that do not require wick insertion into an annular wall to maximize the cost and time savings. The sample also featured a recessed, conical section on the bottom face in order to offset the porous region from the build plate. This offset was introduced deliberately so that the samples could be removed using a wire EDM cutter without slicing through the porous section.

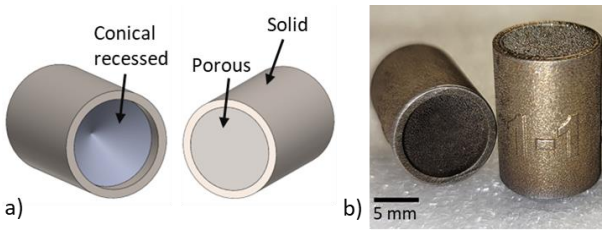

Figure 1: a) Wick sample CAD renderings, and b) 3DP wick samples.

The wick capillary measurements were acquired through a combination of Capillary Flow Porometry (CFP) and Mercury Intrusion Porosimetry (MIP).

Capillary Flow Porometry

The CFP consisted of a bubble-point test to determine the maximum pore radius and a dry gas flow test to determine the wick permeability. In the bubble-point test, the wick sample was first saturated with liquid by submerging it into a bath of Iso-Propyl Alcohol (IPA). The conical end of the sample was then connected to a compressed nitrogen source while the flat end was left submerged in the IPA bath immediately below the level of the liquid, as shown in the schematic presented in Figure 2. Using a pressure regulator, the applied pressure on the conical end was gradually increased until the emergence of the first continuous stream of bubbles from the flat end of the sample, which signaled the breach of the bubble-point pressure. The pressure reading at bubble point was then used in conjunction with Washburn's equation to determine the maximum pore radius, r_{eq}, for a circular pore with an equivalent bubble-point pressure. The IPA bath was removed for the dry gas flow test exposing the sample free end to ambient conditions. The volume flow rate of nitrogen at standard atmospheric conditions was recorded for a range of input pressures. The wick permeability was determined from the acquired measurements using a modified version of Darcy's law to account for the non-traditional sample geometry used in the current study.

Mercury Intrusion Porosimetry

The MIP on the wicks was performed by the Materials Characterization Laboratory at The Pennsylvania State University using a Micrometrics Autopore V series mercury porosimeter. The MIP was conducted to determine the connected porosity of the wick, which controls the heat leak via wick conduction to the evaporator core. It should be noted that the connected porosity includes those pores that are accessible from the surface of the sample. While that includes both the through pores and dead-end pores in the sample, it does not account for the isolated porosity of the sample. Thus, the overall sample porosity is expected to be greater than the MIP connected porosity presented in this paper.

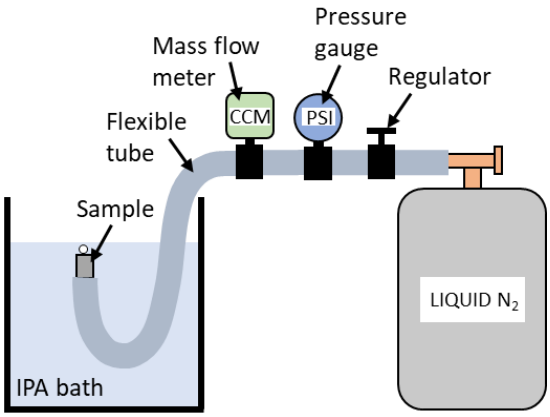

Figure 2: A schematic of the bubble-point test setup.

RESULTS

Wick Development

The results from the wick development effort are summarized in this section. A series of wicks was successfully developed by controlling the build energy density between E_ρ = 1.09 J/mm^3 and E_ρ = 5.08 J/mm^3. At E_ρ = 0.67 J/mm^3, however, the energy density proved to be insufficient for SS powder consolidation, leading to part failure. The acquired capillary measurements from CFP and MIP are summarized in Table 1. All uncertainties presented in this paper span two standard deviations about the mean. From Table 1, an increase in the energy density is associated with a decrease in the magnitude of each capillary variable, as would be intuitively expected. Due to the marginal connected porosity at E_ρ = 5.08 J/mm^3, energy densities beyond this value were not attempted in this effort. A low-permeability wick is associated with increased heat leak via conduction to the evaporator core, leading to diminished thermal performance of the LHP. It should be noted, however, that due to the use of 316L SS as the wick material, the heat leak to the evaporator core even at the lowest connected porosity in Table 1, is expected to be less than the corresponding heat leak through a high-porosity Nickel wick, which is commonly used in standard LHPs.

Table 1. Wick Capillary Measurements

Energy density, E_ρ (J/mm^3)	Max. eq. radius, r_{eq} (µm)	Permeability, k (10^{-14} m^2)	Connected porosity (%)
5.08	2 ± 0.1	0.34 ± 0.01	8.56
3.57	3.03 ± 0.02	1.5 ± 0.1	9.68
2.22	4.09 ± 0.06	2.7 ± 0.2	27.02
1.09	5.94 ± 0.08	49 ± 1	43.97
0.67	Failed		

A major highlight of this effort is the successful development of both a high-capillary-limit wick, with a maximum pore radius of r_{eq} = 2 µm, and a low-density wick, with a porosity of more than 40%. The realization of bi-porous builds, i.e., a single part containing a porous wick and a solid, annular wall, serves as another prominent highlight of this effort. This achievement, in particular, is critical to the development of evaporators as a single part, requiring zero assembly for maximum cost and lead time savings.

A plot of the wick permeability and maximum pore radius is presented in Figure 3. Except when explicitly drawn, the measurement errors are smaller than the marker size in Figure 3. Since a smaller pore radius wick is associated with a lower permeability, the appropriate wick selection for a given application requires consideration of the available pressure margin, i.e., the difference between the wick capillary limit and pressure drop at nominal heat load. The wick porosity serves as another consideration parameter, as a higher porosity wick is expected to offer a better thermal performance than a lower porosity wick due to reasons of heat leak described before. It should be noted that the 3D printing approach offers the flexibility to easily tailor the wick to the desired application as opposed to the standard furnace sintering approach.

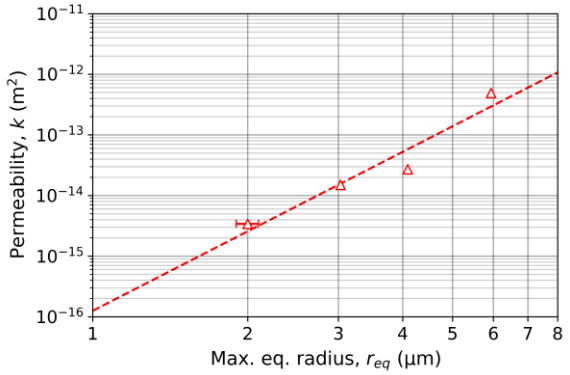

Figure 3: A plot of the maximum pore radius and permeability of the 3DP wicks.

Evaporator Development

The 3DP evaporator was developed with the aim of eliminating all labor-intensive manufacturing steps, including high-risk assemblies. As such, the evaporator is designed to be built as a single part containing a porous wick surrounded by an annular wall. The prior realization of bi-porous wick samples was therefore crucial to enabling the evaporator builds. Figure 4 shows CAD renderings of a 3DP evaporator having a length of l = 0.1 m and an outer diameter of d = 0.025 m. The wick region is shown in white while the surrounding annular wall is shown in grey. The evaporator core, vapor channel, and the vapor grooves can be identified from the sectional view of the wick. The inner and outer wick diameters were set following a numerical analysis to identify the best balance between the heat leak and pressure drop across the wick. Similarly, the vapor groove dimensions were also selected by finding the best balance between the wick thermal conductance and pressure drop whilst adhering to the manufacturing constraints. The circular geometry of the vapor grooves was selected for simplicity.

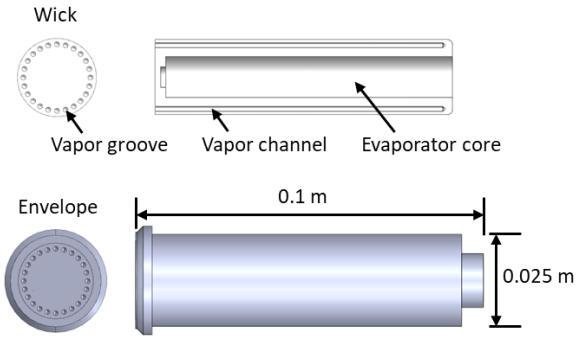

Figure 4: 3DP evaporator CAD renderings.

The thickness of the surrounding envelope was selected to meet the pressure test requirements for flight qualification. Figure 5 shows a photograph of 3DP evaporators built to the specifications of the CAD presented in Figure 4. The evaporator CFP measurements were found to be consistent with the corresponding wick measurements presented in Table 1. Furthermore, the evaporators were inspected radiographically and found to be free from internal cracks and vapor channel blockages. Additionally, these evaporators were also found to be free from leaks following successful tests with a Helium leak checker.

In addition to the evaporators in Figure 5, several other evaporators, spanning an order-of-magnitude in length, were successfully built and inspected, highlighting the scalability that is easily afforded by 3D printing. The smallest evaporator, intended for a potential CubeSat application, is associated with a length of l = 0.04 m,

while the largest, aimed at high-performance SmallSats, has a length of l = 0.25 m.

Figure 5: 3DP evaporators built to the specifications of the CAD presented in Figure 4.

Baseline Testing

The testing of the 3DP evaporators was conducted in the laboratory environment for various different heat loads, sink conditions, working fluids, gravity conditions, etc. A liquid nitrogen-cooled cold plate attached to the condenser served as the sink in these tests. A selection of the test results is presented in this section.

The baseline propylene and ammonia LHP tests were conducted using the 0.1 m long evaporator shown in Figure 5. This evaporator featured a wick with a maximum pore radius of $r_{eq} \approx 6$ µm, permeability of $k \approx 5 \times 10^{-13}$ m^2, and porosity of 44%. A standard screen-based secondary wick was used to hydraulically connect the evaporator and the compensation chamber. A CAD rendering and photograph of the assembled LHP that was used for testing for both the propylene and ammonia cases are presented in Figure 6. The LHP fluid lines were built using 316L SS tubing with an outer diameter of d = 3.175 mm. The condenser line was arranged along a serpentine path covering a total length of l = 3.5 m. For heating, the evaporator was placed inside a saddle, which was in turn, installed on a heater block containing several cartridge heaters. For both the propylene and ammonia baseline tests, the sink temperature was held constant at T_s = 0 °C. The baseline tests were conducted with the LHP placed horizontally to eliminate the influence of gravity.

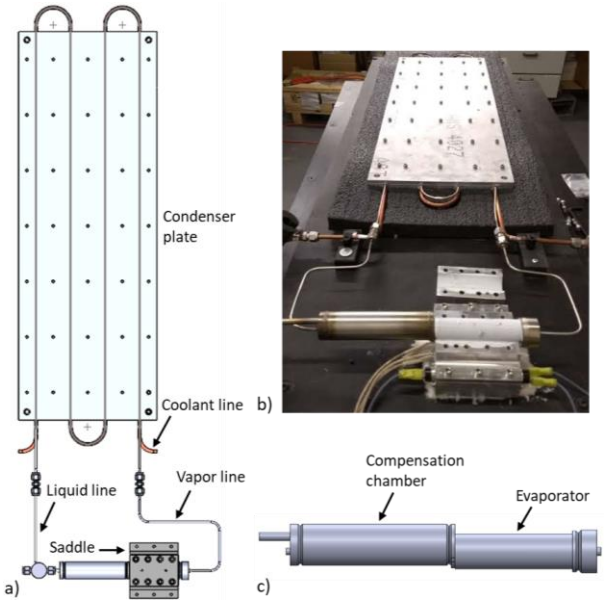

Figure 6: a) A CAD rendering of the LHP used for testing, b) a photograph of the assembled LHP in the laboratory, and c) a rendering of the evaporator and compensation chamber assembly.

The baseline propylene test results are presented in Figure 7. The heat load was increased in 5-10 W steps, but testing was stopped due to time limitations at Q = 85 W. The temperature difference, ΔT, between the evaporator surface and the exit of the vapor channel is shown using black markers in Figure 8. The major contributions to this temperature difference stem from the thermal resistance of the annular wall and the evaporative resistance in the vapor grooves. This temperature difference was used to define an evaporator conductance which is shown using blue markers in Figure 7. The drop in conductance with increasing heat load is believed to mainly occur due to a partial dry out in the evaporator.

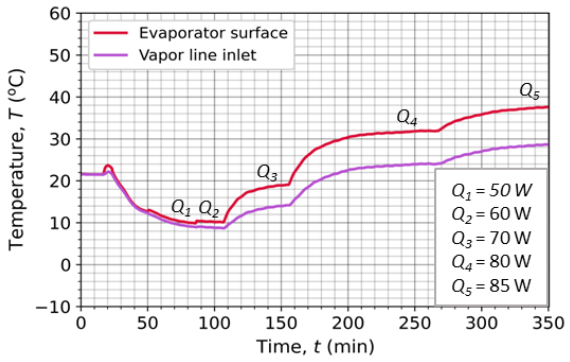

Figure 7: Propylene LHP baseline test results at 0 °C constant sink.

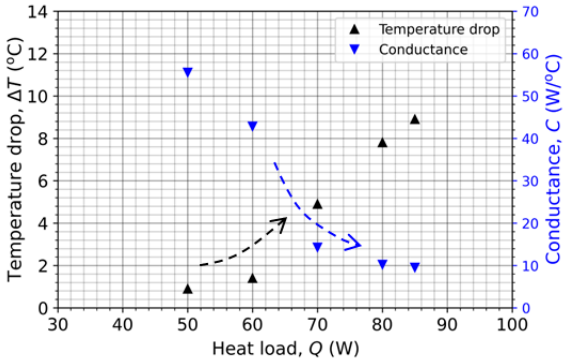

Figure 8: Evaporator surface-to-vapor exit temperature difference and conductance corresponding to the results presented in Figure 7.

The baseline ammonia test results are presented in Figure 9. As expected, the ammonia LHP was able to transport a much higher heat load than the propylene system. The step-up heat application was stopped at a heat load of Q = 300 W without any indications of a complete evaporator dry out. The evaporator surface-vapor exit temperature difference and the corresponding evaporator conductance for the ammonia LHP are presented in Figure 10. The conductance is found to be overall greater than the propylene LHP due to the significantly higher latent heat of vaporization of ammonia, which enables a higher heat transfer rate despite a similar pressure drop in the system.

The operational demonstration at a heat load of Q = 300 W with a 0.1 m long evaporator is a major highlight of the current effort as it can enable high-performance future SmallSats with significantly higher heat rejection capability than the current state of the art. As an example, the heat rejection of a standard ESPA-class satellite can be more than doubled by installing a deployable radiator for each body-fixed radiator using the 3DP LHP as the thermal link.

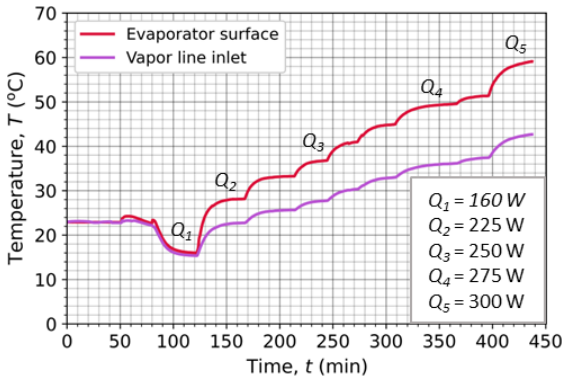

Figure 9: Ammonia LHP baseline test results at 0 °C constant sink.

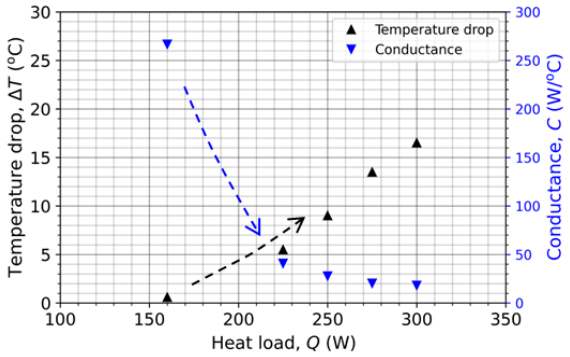

Figure 10: Evaporator surface-to-vapor exit temperature difference and conductance corresponding to the results presented in Figure 9.

NASA VIPER EDU

A propylene 3DP-LHP was designed and built for NASA's VIPER EDU testing. The VIPER mission aims to send a lunar rover to investigate volatiles on the lunar south pole. ACT was tasked with building the thermal management architecture for VIPER. The 3DP-LHP was developed in parallel with the flight hardware solely for the purposes of EDU testing.

A CAD rendering of the LHP is presented in Figure 11. A photograph of the LHP installed in the shipping rack is presented in Figure 12. The system sizing and configuration was done to meet the specified mission requirements, including conforming to the specified geometry for installation on the rover. The LHP was equipped with an evaporator that is identical to the one used for baseline testing. The evaporator dimensions, in particular the length of l = 0.1 m, were deemed appropriate for the spatial constraints imposed on the system. As a reminder, the evaporator wick is associated with a maximum pore radius of $r_{eq} \approx 6$ µm, permeability of $k \approx 5 \times 10^{-13}$ m^2, and porosity of 44%.

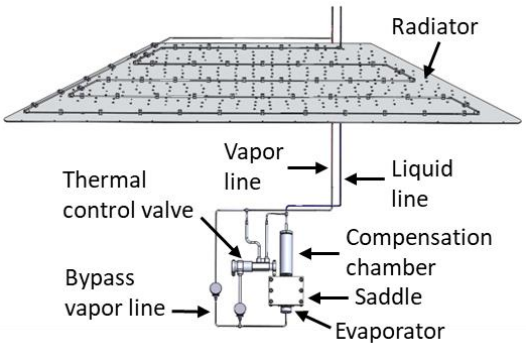

Figure 11: A CAD rendering of the 3DP-LHP for NASA's VIPER EDU testing.

The fluid lines were once again constructed using SS tubing with an outer diameter of d = 3.175 mm. It should be noted that the fluid lines for the LHP had a combined length of l = 11 m, which is significantly longer than the LHP that was used previously for baseline testing. A thermal control valve was also installed in the LHP on the vapor line to prevent heat leak during lunar nights. However, the results presented in this section correspond to testing in the laboratory that was conducted only via the bypass vapor line, which is indicated in Figure 11.

Figure 12: A photograph of the VIPER 3DP-LHP installed in the shipping rack.

The results from testing of the VIPER propylene LHP at a constant sink temperature of T_s = 0 ºC are presented in Figure 13. As with the baseline testing, the heat load was increased in well-defined steps up to a value of Q = 70 W, which is 20 W more than the heat load expected during the mission.

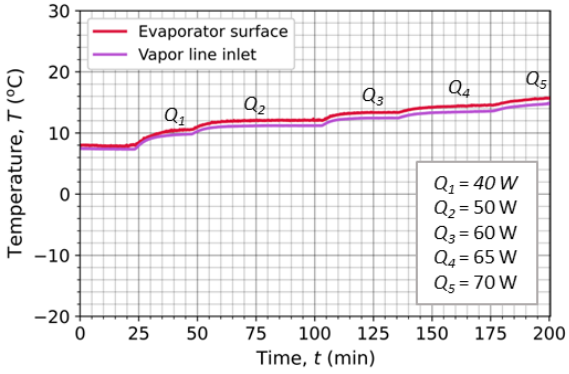

Figure 13: VIPER propylene LHP laboratory test results at 0 ºC constant sink.

The evaporator surface-vapor exit temperature difference and the evaporator conductance are presented in Figure 14. The temperature difference shows marginal increase with increasing heat load, leading to an overall increase in the conductance. This result is in sharp contrast with the baseline propylene LHP result presented in Figure 8, which shows a significant drop in the conductance. The difference can be attributed to the gravity assist resulting from the significant gravity head in the case of the VIPER LHP.

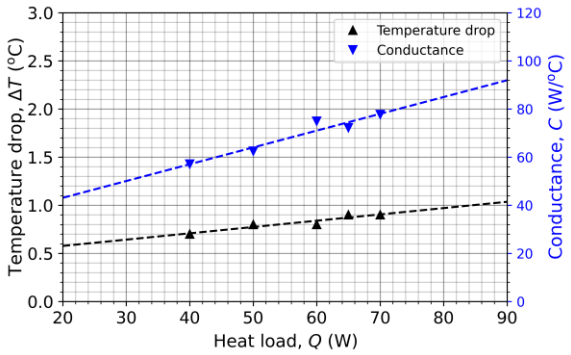

Figure 14: Evaporator surface-to-vapor exit temperature difference and conductance corresponding to the results presented in Figure 13.

The 3DP-LHP is currently associated with a TRL of 6 following the successful demonstration of the propylene LHP for NASA's VIPER EDU. Current efforts are aimed at improving the thermal conductance of the system via improvement of the vapor groove design using non-circular geometry.

Acknowledgments

This work was funded by NASA through the Small Business Innovation Research (SBIR) program under contracts 80NSSC21C0563 and NNX17CM09C. The authors would like to acknowledge Adam Shreve, Dave Carlson, and Dennis Winters for their significant contributions with fabrication, assembly, and testing.

References

1. Richard, B., Anderson, W., Chen, C.-H., Crawmer, J., and Augustine, M., "Development of a 3D Printed Loop Heat Pipe," *49th International Conference on Environmental Systems*, Boston, Massachussets, 2019.
2. Gupta, R., Chen, C-H., and Anderson, W.G., "Progress on 3D Printed Loop Heat Pipes," *50th International Conference on Environmental Systems*, 2021.
3. Gupta, R., Chen, C-H., and Anderson, W.G., "Experiments on a Loop Heat Pipe with a 3D Printed Evaporator," *51st International Conference on Environmental Systems*, 2022.
4. Mezghani, A., Nassar, A.R., Dickman, C.J., Valdes, E., and Alvarado, R., "Laser Powder Bed

Fusion Additive Manufacturing of Copper Wicking Structures: Fabrication and Capillary Characterization," *Rapid Prototyping Journal*, Vol. 27, No. 6, 2021, pp. 1181-1188.

5. Gotoh, R., Furst, B.I., Roberts, S.N., Cappucci, S., Daimaru, T., and Sunada, E.T., "Experimental and Analytical Investigations of AlSi10Mg, Stainless Steel, Inconel 625 and Ti-6Al-4V Porous Materials Printed via Powder Bed Fusion," *Progress in Additive Manufacturing*, Vol. 7, No. 5, 2022, pp. 943-955.